Chapter 6

EXPERIMENTAL VERIFICATION

To verify the capabilities and to study the limitations of the image processing modules, experiments were performed on actual passenger luggage. These bags were bought from US Air. There are two parts to this verification. The first part is to verify the image segmentation module. The second part is to verify the module for determining an object's *true* gray levels.

Using these 20 bags that were obtained from US Air, by inserting different objects, over 100 experimental scenarios were created. The objects that were inserted in the bags include: explosive simulants, a white plastic step wedge, an aluminium step wedge, a Walkman cassette player, shampoo bottles, hair dryers, pillows, clothes, towels, books, quilts, etc. For each scenario, a set of images was collected using the modified AS&E 101ZZ system. Each set included a high-energy transmission image, a low-energy transmission image, a low-energy forward-scatter image, and a low-energy backscatter image of the bag. The image-processing system was then tested on these bag images. Figure 6-1 shows the outward appearance of a typical bag. Figure 6-2 shows some of the contents that are placed inside.

Figure 6-1 Outward appearance of a passenger luggage bag.

Figure 6-2 Contents of the bag shown in Figure 6-1.

This study focused on detecting explosives in luggage. But using real explosives as experimental test objects pose serious safety concerns at a university. The SDA Lab does not have the necessary means to obtain, transport, and store these hazardous materials. However, to perform meaningful experiments some types of illicit materials must be used for experimentation. Explosive simulants are the proper substitutes for real explosives. Explosive simulants are inert materials that exhibit accurately controlled physical properties. They specifically and reliably duplicate selected characteristics such as *density* and Z_{eff} of real explosive material, and those characteristics are recognized by specific explosive material detection technology such as x-ray technologies [SPA96]. Using simulants, the safety was greatly increased while the simplicity of handling objects for testing have been greatly improved.

Early simulants were rigid plastics [SPA96]. They have limited usefulness in accurately simulating explosive devices, training operators, and testing automated detection systems that use x-rays. The simulant objects used in this study's experiments are listed in Table 6-1. Simulant 7 to 10 are all the early type of rigid plastic simulants. They have similar Z_{eff} to the real explosives, but do not have the same *density*.

Simulants 1 through 6 are all members of a new class of explosive simulants. These simulants are physical mixtures of two or more components. The components' inert properties have all been verified by analyses and none of these components is regulated by the government. The components have minimal acute toxicity hazard levels or none at all. They match both the Z_{eff} and *density* of actual explosives. Also since they are all powders, this makes them like real explosives as well. All these simulants have demonstrated stability of over 6 months when they are appropriately wrapped and packed.

Figure 6-3 shows pictures of those 10 types of simulants that were used in the study. This figure also shows the containers that were used for the new class of explosive simulants.

Table 6-1 List of standard explosive simulants used in my study

Simulant #	Simulant Name	Descriptions
1	RXN-06-AF	Powder in a plastics container
2	RXN-06-AF	Powder in plastic wrap
3	RXN-11-GE-AB	Powder in a plastics container
4	RXN-07-AE	Powder in a plastics container
5	RXN-08-AJ	Powder in a plastics container
6	RXN-10-GE-AF	Powder in a plastics container
7	Plastics #1	Solid square plastics object
8	Plastics #2	Solid square plastics object
9	Plastics #3	Solid square plastics object
10	Plastics #4	3 solid cylinder object bundle

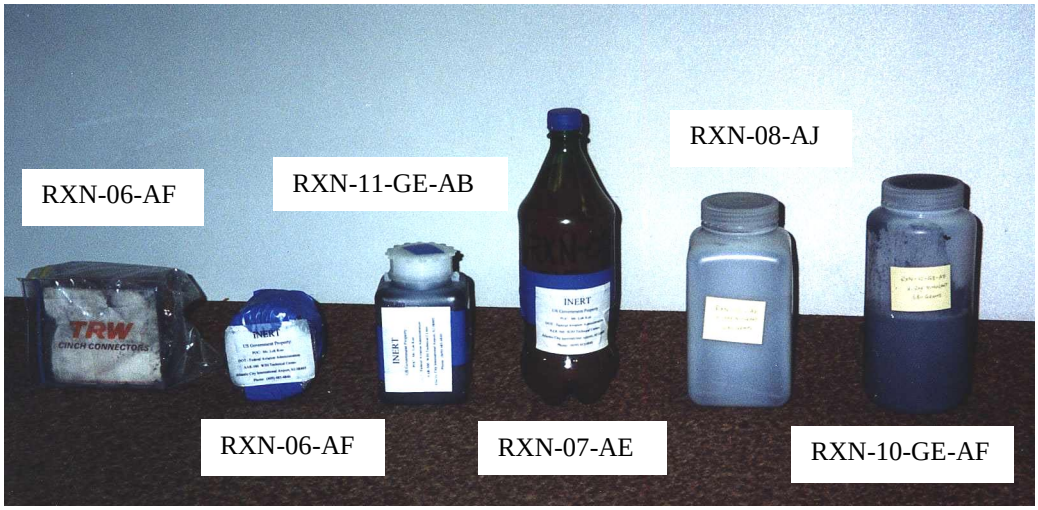

(a)

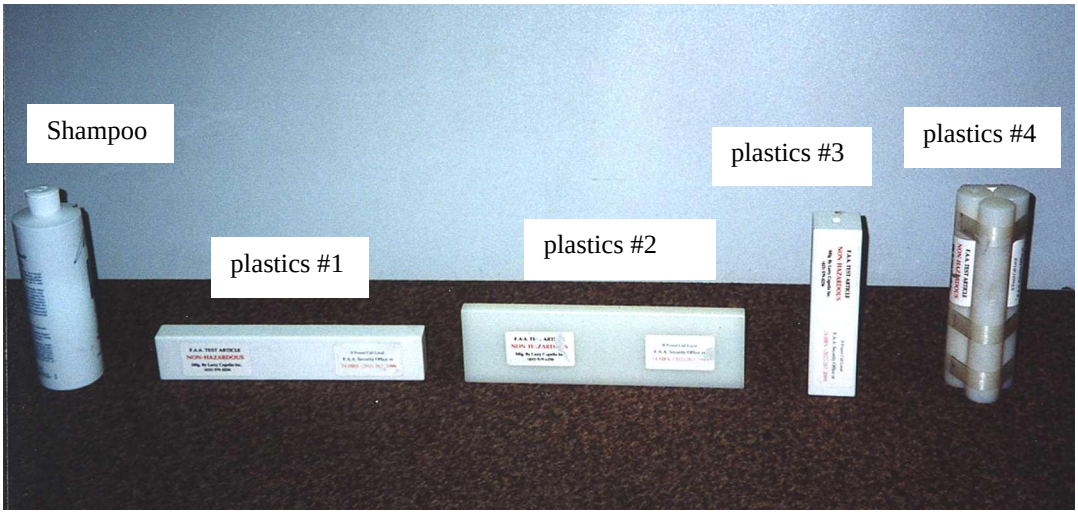

(b)

Figure 6-3 Photos of the 10 types of explosive simulants used in my study. (a) RXN type simulants; (b) Plastics types of simulants.

Besides these explosive simulants, other types of test objects are also used for this study. These include plastic, aluminum, and steel step wedges. Honey, sugar, water, and shampoo, all packed in plastic containers, were also used in experiments. These objects have similar Z_{eff} and *density* to the real explosives and are difficult to differentiate from explosive compounds.

Routine *registration()* works properly on 98% of the image sets. This routine calls a number of subroutines including *cut_hist()* to perform the registration operation. In some occasions, routine *cut_hist()* found the wrong left or right boundaries of a bag in a high-energy transmission image.

Figure 6-4 shows a bag image in high-energy transmission modality whose bag boundaries were not correctly identified. Figure 6-4 (a) is the bag image obtained from the AS&E system. The image has been shading corrected. Figure 6-4 (b) is the minimum-inscribing rectangle region of the bag that was obtained by applying *cut_hist()*. This rectangle was not correctly found. There may be several factors that contribute to the failure of routine *cut_hist()*. One can easily see that the image has significant noise. The contrast between the pixels on the left bag boundary and the pixels of the background is too small. Those two factors have severely degraded the ability of *cut_hist()* to find the correct histogram threshold that separates the background image from the foreground region near the left boundary.

The algorithm itself is believed to have already done a reasonable job in finding the boundaries of the minimum-inscribing rectangle. The problem more lies on the image collection hardware. Figure 6-5 shows the gray level variation of a row of air image in image Figure 6-4 (a). Normally the gray levels of a row of air image should not have much variation. The variation shown here has been over 20 gray levels. There are many reasons that may cause this variations and noise in the system. It is up to the hardware people to really fix those problems. These noise and variations are believed to be the real problems that cause the *cut_hist()* to fail occasionally. The hardware must be improved before perfect boundary findings can be achieved.

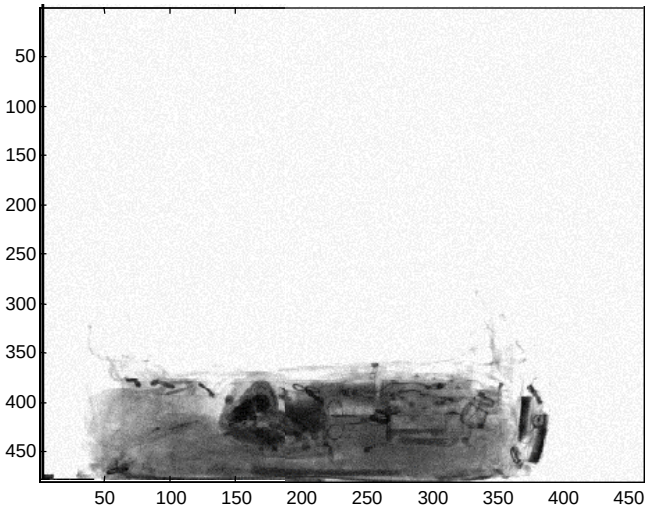

(a)

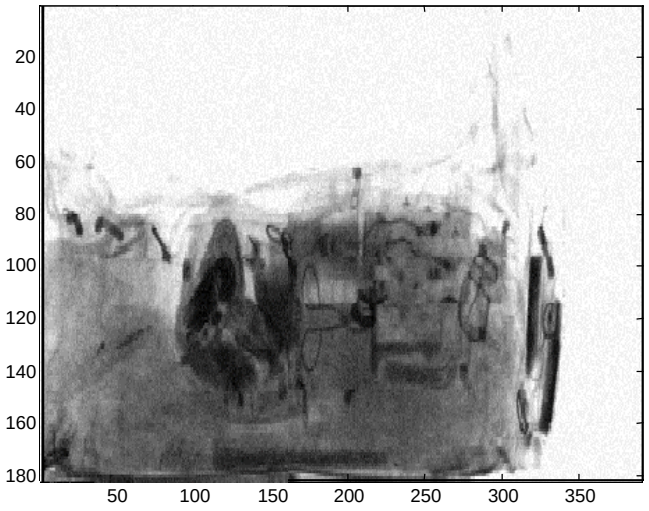

(b)

Figure 6-4 Illustration of the failure of routine *cut_hist()*. (a) a high-energy transmission image obtained from the AS&E system after shading correction; (b) the image after applying routine *cut_hist()* to find the bag's boundary.

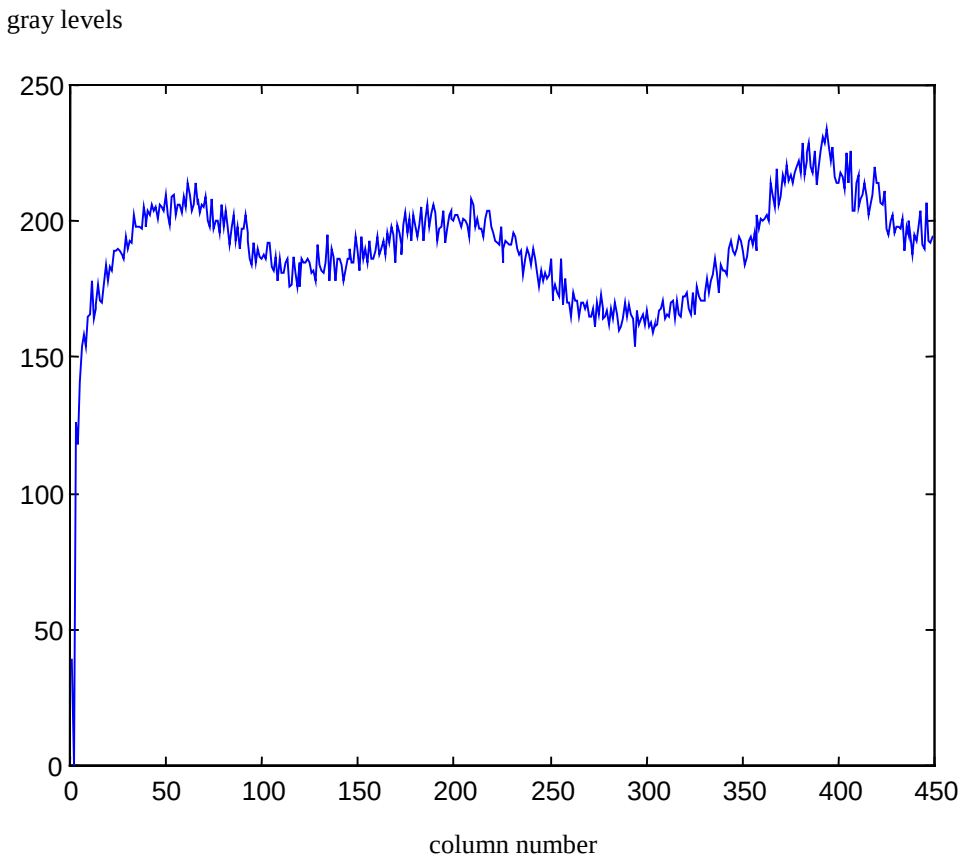

Figure 6-5 Gray levels of pixels at row 30. The image examined is Figure 6-4 (a).

Routine *segmentation()* works properly on all image sets. For all the images that were examined, *solid* objects are properly segmented into relatively large regions. Each region in Img_{Rgn}^{Lbl} has relatively uniform gray levels while the geometry of each region in Img_{Rgn}^{Obj} is closer to an object. Some of the segmentation results have been shown earlier in Section 4.3. Some more results are shown in this chapter.

Figure 6-6 shows the segmentation results of a simple environment. In Figure 6-6 (a), the low-energy transmission image contains a bottle, two books, and two step wedges. The segmentation result is shown in Figure 6-6 (b). The threshold used in this segmentation is 3. The segmentation result is quite accurate. Each step of a step wedge is segmented into a different region. The parts of the book that are not overlapped with step wedges are properly segmented into separate regions. The middle part of the bottle where the gray level transition is relatively small is segmented into one big region. Using threshold 5, the resulted labeled image is similar to Figure 6-6 (b), so it is not shown here. Those two segmented images are similar because of the large gray level contrast between neighboring regions in this low-energy transmission image.

Figure 6-7 shows the segmentation results of a simple bag image. Figure 6-7 (a) is a low-energy transmission bag image. Inside the bag, there is an aluminum step wedge and a pillow that has roughly the size of the bag. The segmentation was done using a threshold of 3. The segmentation result is quite good. Each step of the step wedge is properly segmented into a region. The pillow that is stuffed in the bag is segmented into a big region. Again the segmented image that uses threshold 5 is not shown in here. The two segmented images are similar to each because of the same reason stated above.

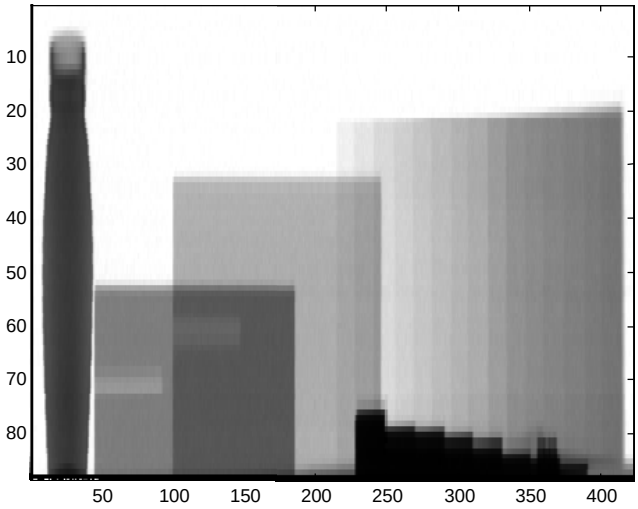

(a)

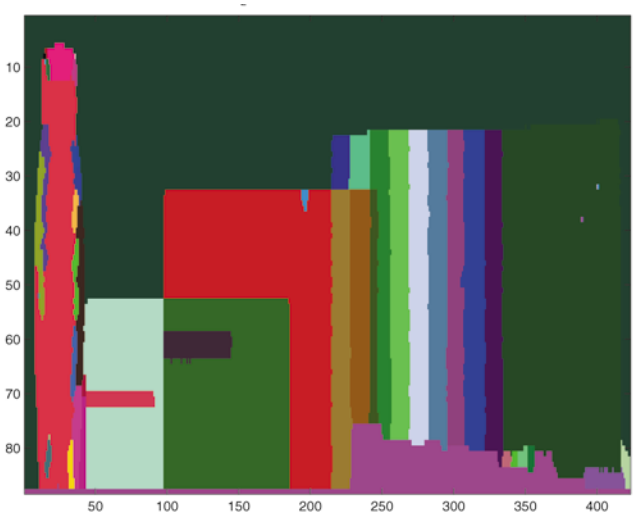

(b)

Figure 6-6 Illustration of applying routine *segmentation()* to a simple environment. (a) The low-energy transmission image of a bottle, two books, and two step wedges. (b) The segmentation results.

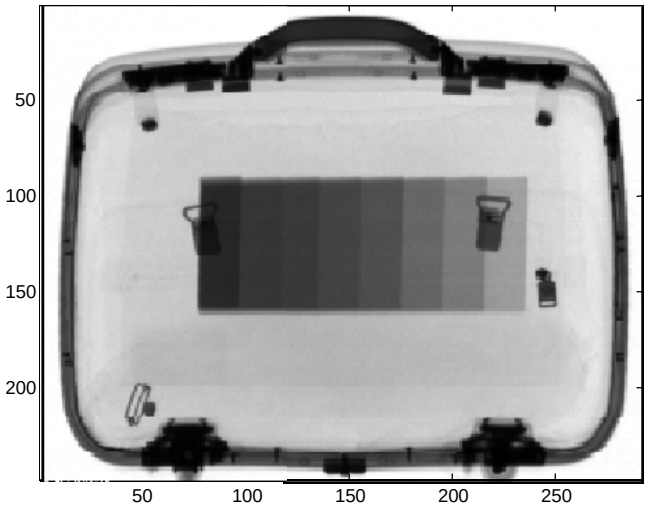

(a)

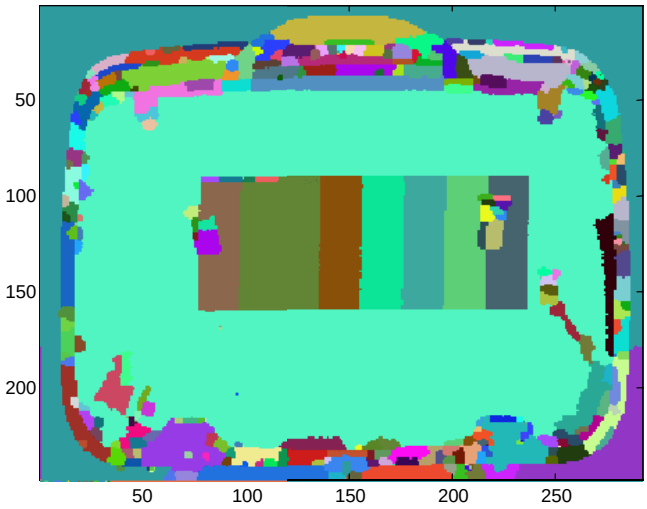

(b)

Figure 6-7 Illustration of applying *segmentation()* to a relative simple bag image. (a) The low-energy transmission image of the bag. The bag contains two objects: a step wedge and a pillow that has the size of the bag. (b) The segmentation result.

Figure 6-8 shows the segmentation results of a more complicated bag image. Figure 6-8 (a) is the low-energy transmission bag image. Inside this bag, there are a pair of shoes, a bottle that contains explosive simulant, and a round shape object that is explosive simulant. Figure 6-8 (b) shows the segmentation result that is using a threshold of 3. The segmentation result is quite accurate in segmenting those *solid* objects. The bottle was segmented into a large region along with several smaller regions. This bottle can be seen completely segmented into one large region in Figure 6-8 (c), where a threshold of 5 was used. Each shoe was segmented into many smaller regions in Figure 6-8 (b). But each shoe was segmented into a large region along with some smaller regions in Figure 6-8 (c). The segmentation results are quite satisfactory.

Generally speaking, the segmentation algorithm performed very well on images that contain very simple objects to images contain very complicated objects. The algorithm is quite stable in generating the segmentation results, results will not vary from one segmentation to another for the same image. The speed is fast. It is a good segmentation algorithm for x-ray bag images.

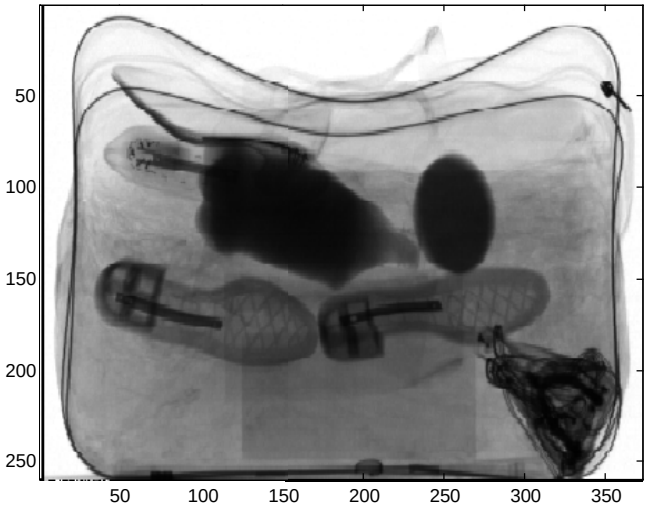

(a)

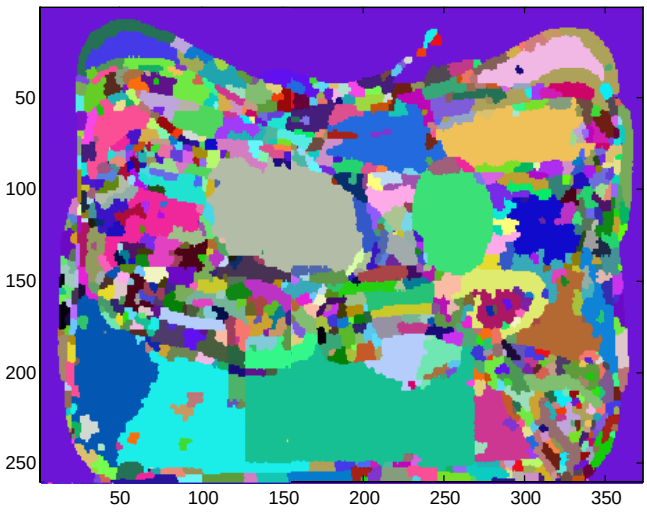

(b)

Figure 6-8 Illustration of applying *segmentation()* to a more complicated bag image. (a) The low-energy transmission bag image. Inside the bag, there are a pair of shoes, a bottle that contains explosive simulant, and a round shape object that contains explosive simulant. (b) The segmented labeled image using a threshold of 3. (Continued to next page)

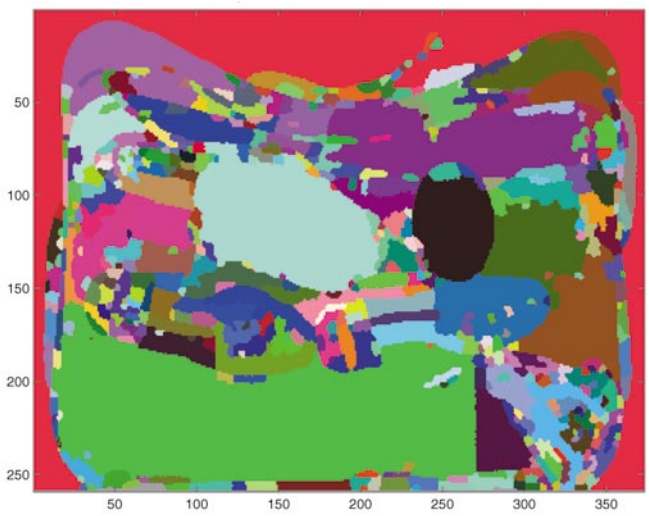

(c)

Figure 6-8 (c) The segmented labeled image using a threshold of 5.

Now, a complete registration and segmentation result for one bag in all four sensing modalities is shown. This might give readers a complete view of the segmentation module. Figure 6-9 shows the images that were collected from the AS&E system. Note that those images were already shading corrected. Figure 6-10 shows the images after applying routine *registration()*. Those images were properly registered. Figure 6-11 illustrates the contents in this bag. Figure 6-12 shows the images after applying routine *smoothing()*. Figure 6-13 shows the segmentation results for the low-energy transmission image. Those two segmented images are spatially registered to the rest four smoothed images.

The registration and segmentation procedures usually take about 40 to 80 secs to execute; and the exact speed depends on the size of the image to be processed. The running speed can be significantly improved by using new computing hardware and without making major modifications to the algorithms.

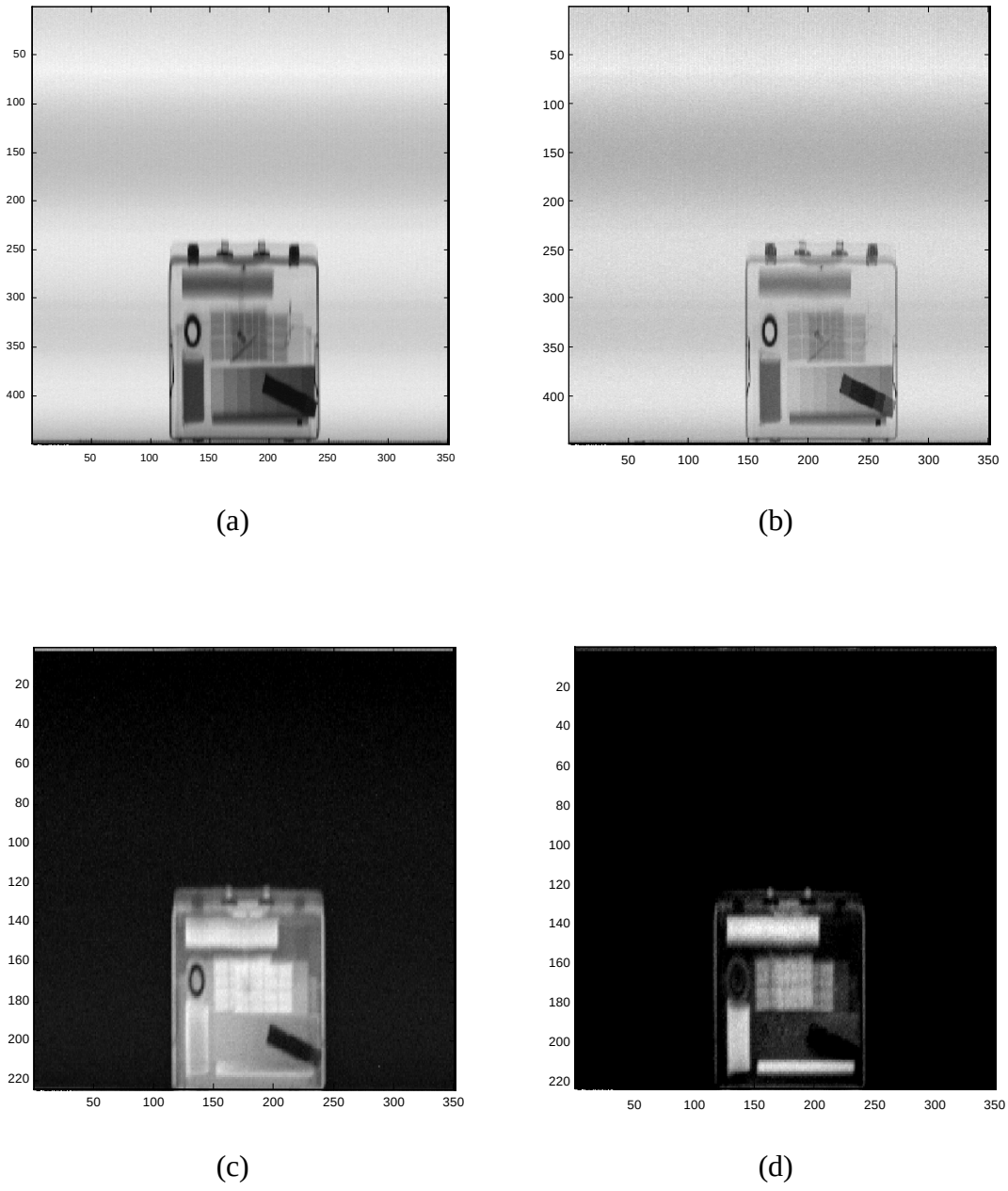

Figure 6-9 Images that were collected from the AS&E system. Note: forward scatter and backscatter images have the correct image geometry because their geometry was adjusted during scanning. a) Low-energy transmission image Img^{L}; b) High-energy transmission image Img^{H}; c) Forward-scatter image Img^{F}; and d) Backscatter image Img^{B}.

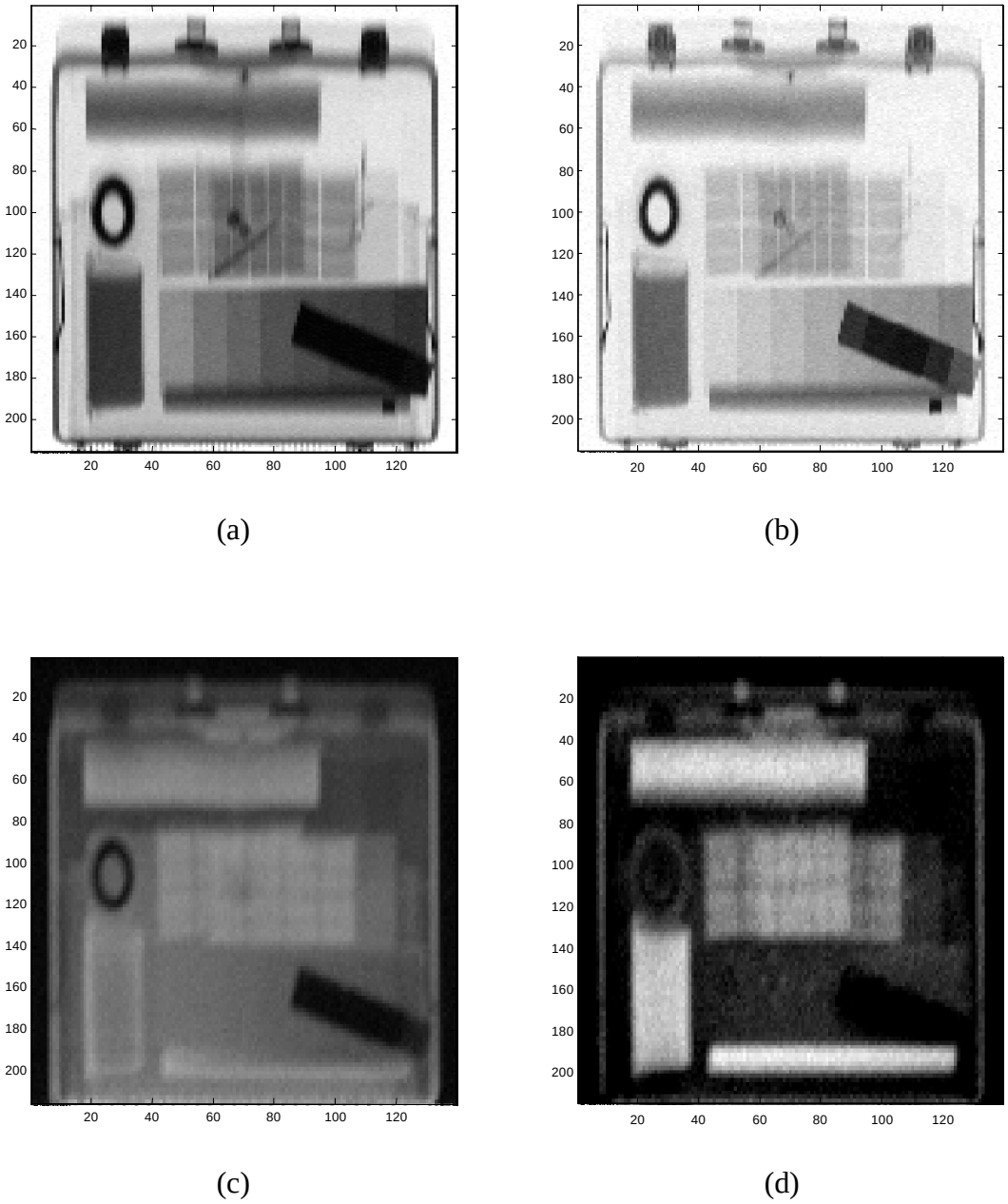

Figure 6-10 Registration results by using minimum-inscribing rectangle cutting method, foreground objects in different sensing modalities are registered. a) Low-energy transmission image Img_{Cut}^{L}; b) High-energy transmission image Img_{Cut}^{H}; c) Forward scatter image Img_{Cut}^{F}; d) Backscatter image Img_{Cut}^{B};

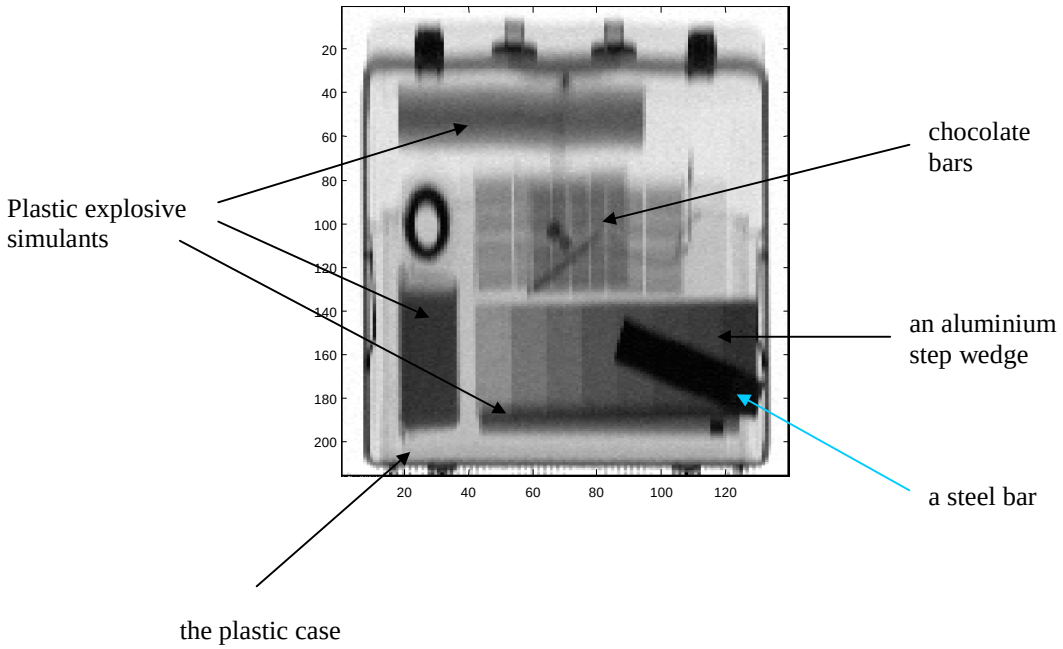

Figure 6-11 Objects appearing in a plastic bag.

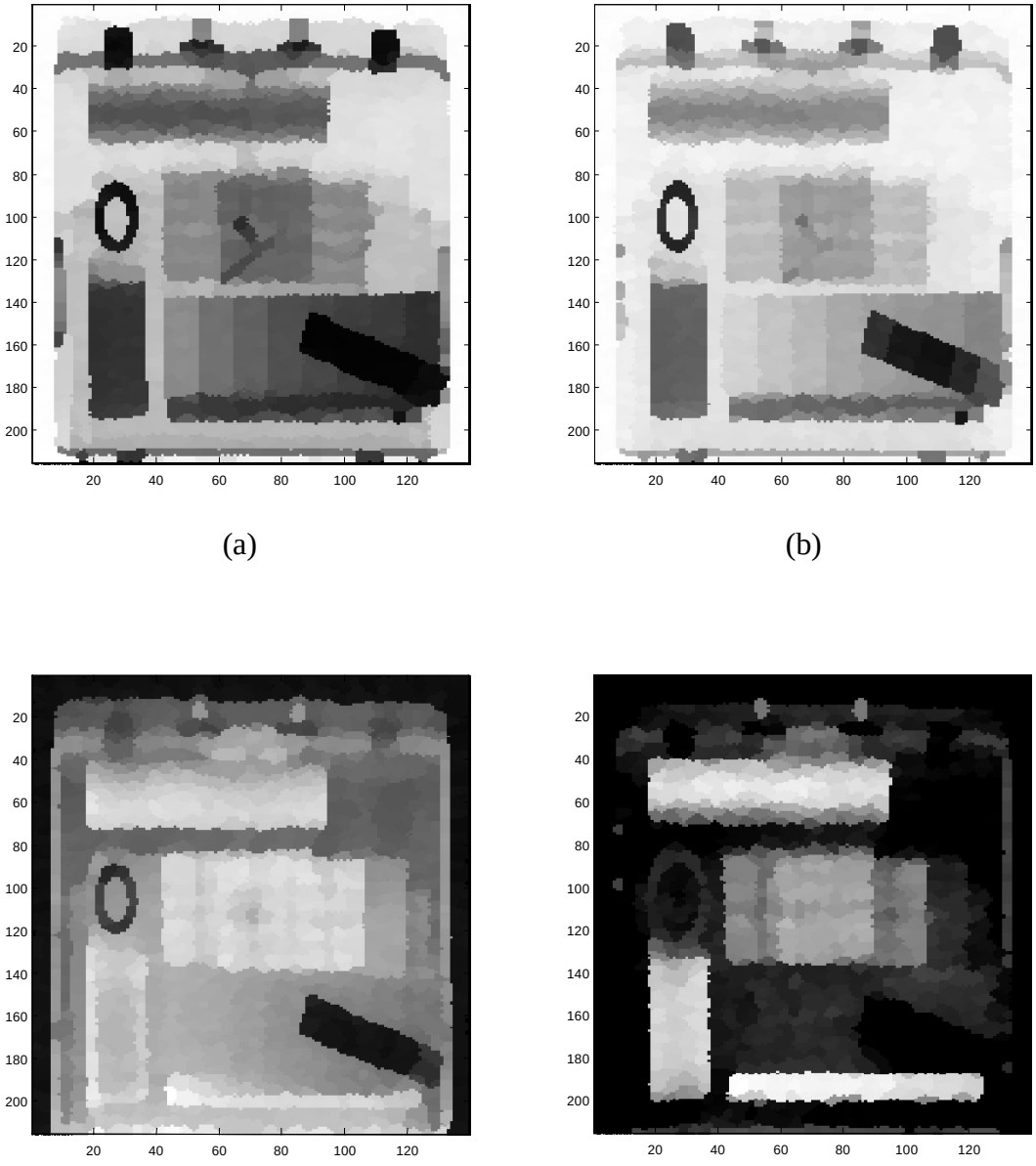

Figure 6-12 Image smoothing results. a) Low-energy transmission image Img_{Smth}^{L}; b) High-energy transmission image Img_{Smth}^{H}; c) Forward-scatter image Img_{Smth}^{F}; and d) Backscatter image Img_{Smth}^{B}.

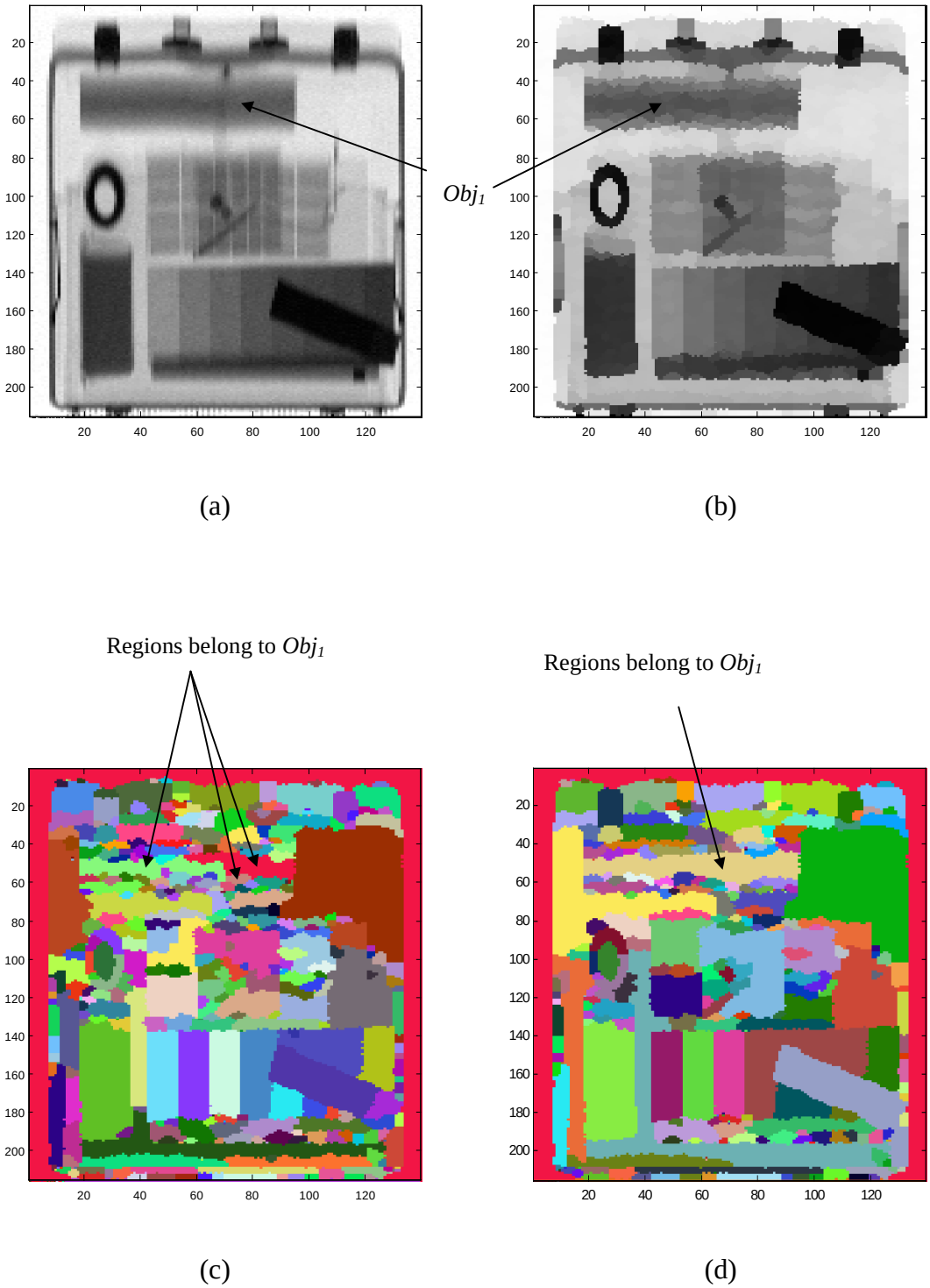

Figure 6-13 Image segmentation results. a) Low-energy transmission image Img^{L}_{Cut}; b) Smoothed image Img^{L}_{Smth}; c) Region label image Img^{Rgn}_{Lbl}; and d) Object label image Img^{Obj}_{Lbl}.

Routine *true_gl()* is verified on object bases. In a test image, there are usually 4 to 10 objects that are *solid* objects. The computed *true* gray levels are compared with the measured *true* gray levels for those *solid* objects. Each object of one detection environment is considered as a data set. Overall over 400 data sets are examined. Some of the results are shown in Table 6-2. The environments that objects were placed for the experiments were shown in from Figure 6-14 to Figure 6-19. The first column of this table describes the object that is being examined and the environment in which it is placed. The image that the object was placed was also indicated for most of the test objects. The second column shows the computed *true* gray levels of this object. The third column shows the measured *true* gray levels of this object. The fourth column shows the computation errors.

For example take row 1. The object being examined is a step of an aluminum step wedge. This step wedge was placed in a plastic luggage bag as seen in Figure 6-14. A pillow is inserted behind the step wedge. The computed *true* gray level is 49 in high-energy transmission modality and 83 in low-energy transmission modality. The measured *true* gray level is 52 in high-energy transmission modality and 91 in low-energy transmission modality. The errors are 5.7% in high-energy transmission modality and 8.8% in low-energy transmission modality.

We have observed that most of the computed *true* gray levels have errors less than 5%. Considering that the system noise for the transmission image collection is about that much, the computation is reasonably accurate.

Table 6-2 Comparison between computed and measured *true* gray levels

Object Description	Computed (g^L, g^H)	Measured $(\tilde{g}^L, \tilde{g}^H)$	Errors $((\tilde{g}^L - g^L)/g^L,$ $(\tilde{g}^H - g^H)/g^H)$
Step 1 of the aluminum step wedge seen in Figure 6-14	(49, 83)	(52, 91)	(5.7%, 8.8%)
Step 2 of the step wedge as seen in Figure 6-14	(69, 109)	(73, 119)	(5.5%, 8.4%)
Step 3 of the step wedge as seen in Figure 6-14	(84, 125.7)	(90, 136)	(6.7%, 7.6%)
Step 4 of the step wedge as seen in Figure 6-14	(98.6, 140)	(104, 149.8)	(5.2%, 6.5%)
Step 5 of the step wedge as seen in Figure 6-14	(127.4, 167.6)	(132.7, 176)	(4.0%, 4.8%)
Step 6 of the step wedge as seen in Figure 6-14	(153.8, 189.8)	(157, 195)	(2.0%, 2.7%)
Step 7 of the step wedge as seen in Figure 6-14	(197, 223)	(197, 223)	(0.0%, 0.0%)
simulant #1 in a passenger bag made of man-made fiber, filled with clothes and other objects as seen in Figure 6-15	(27, 41)	(25, 43)	(8.0%, 4.7%)
simulant #2 in a rigid plastics passenger bag filled with clothes as seen in Figure 6-15	(45, 57)	(43.5, 59)	(3.5%, 3.4%)
simulant #9 in the same environment as seen in Figure 6-15	(76, 87.8)	(78, 93.7)	(2.6%, 6.3%)
shampoo bottle in a rigid plastic bag as seen in Figure 6-16	(75, 92)	(72.7, 89)	(3.2%, 3.4%)
simulant #1 in Figure 6-16	(22, 38)	(27, 40)	(19.0%, 5.0%)
simulant #7 in Figure 6-16	(124, 139)	(124, 140)	(0.0%, 0.7%)
simulant #10 in Figure 6-16	(122, 135)	(123, 140)	(0.8%, 3.6%)
simulant #2 in soft plastic bag that contains many clothes, glass bottles, and simulants as seen in Figure 6-17	(45, 59)	(43, 59)	(4.7%, 0.0%)
simulant #9 in Figure 6-17	(74, 91)	(78, 99)	(5.1%, 8.1%)
simulant #2 in Figure 6-17	(42, 53)	(43, 59)	(2.3%, 10.2%)

Object Description	Computed (g^L, g^H)	Measured $(\tilde{g}^L, \tilde{g}^H)$	Errors $((\tilde{g}^L - g^L)/g^L,$ $(\tilde{g}^H - g^H)/g^H)$
a shampoo bottle in a cotton carry-on bag filled with shoes, clothes, detergent, and etc. as seen in Figure 6-18	(82, 99)	(72.7, 89.4)	(12.8%, 10.7%)
book in a rigid plastics passenger bag filled with clothes as seen in Figure 6-19	(160, 175)	(165, 185)	(3.0%, 5.4%)
simulant #5 in a cotton carry-on bag filled with clothes, books in Figure 6-19	(30, 44)	(27, 40)	(11.1%, 10.0%)
simulant #1 in a plastics bag (bag image is not shown)	(54, 78)	(57, 83)	(5.3%, 6.0%)
simulant #1 in a plastics bag with a different orientation (bag image is not shown)	(21, 33)	(19, 35)	(10.5%, 5.7%)
simulant #8 in the same environment (bag image is not shown)	(172, 183)	(173, 183)	(0.6%, 0.0%)
simulant #1 in a rigid plastics passenger bag filled with a pillow and some fluid bottles (bag image is not shown)	(64, 88)	(57.5, 83)	(11.3%, 6.0%)
simulant #2 in a plastics bag (bag image is not shown)	(43, 58)	(43.5, 59)	(1.2%, 1.7%)

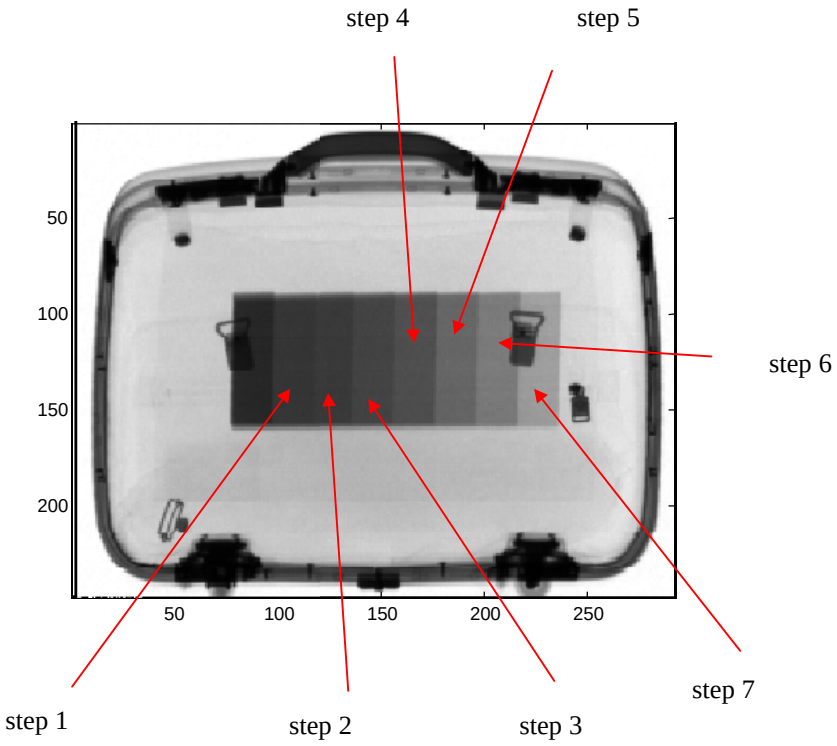

Figure 6-14 Low-energy transmission image of a bag that contains an aluminium step wedge and a pillow. This pillow has roughly the size of the bag and had filled the entire bag.

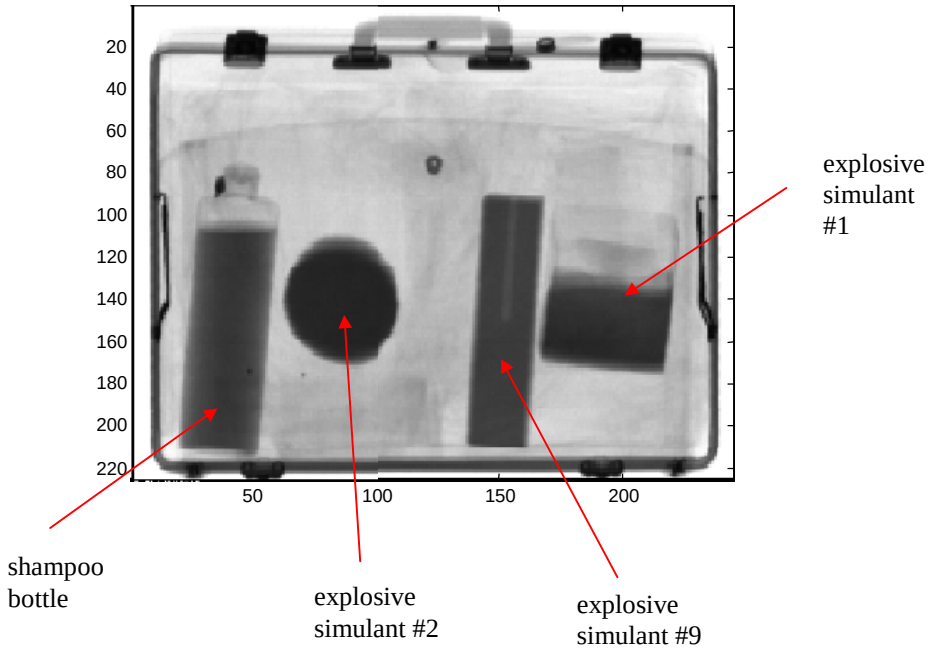

Figure 6-15 Low-energy transmission image of a bag. This bag contains four *solid* objects: a shampoo bottle, and three explosive simulants. The bag is filled with clothes and towels.

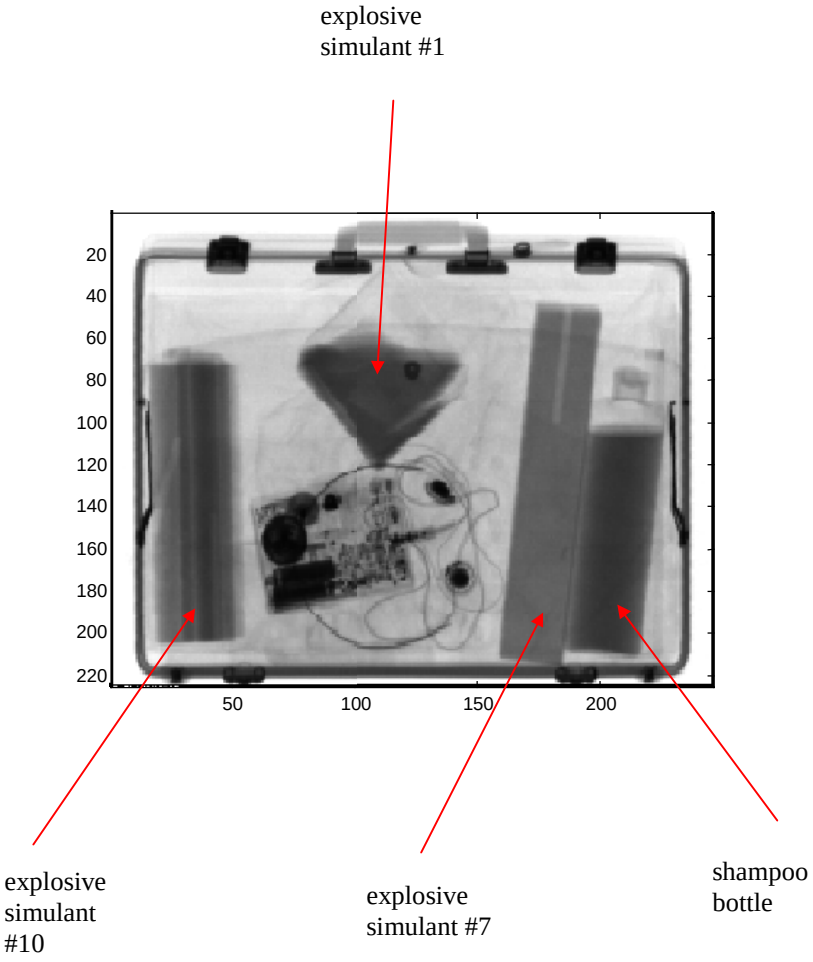

Figure 6-16 Low-energy transmission image of a rigid plastic bag that contains explosive simulants and a shampoo bottle. The rest of the bag is filled with clothes and towels.

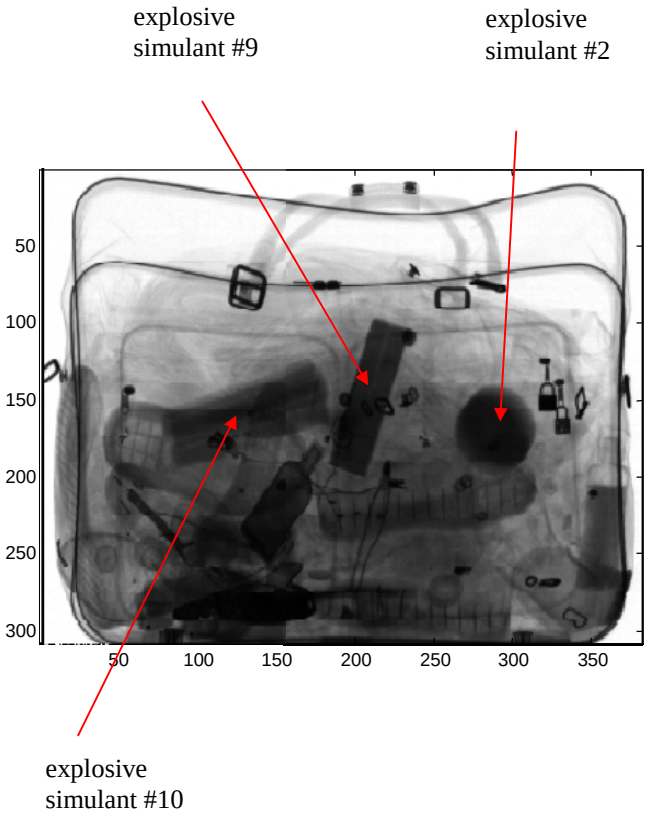

Figure 6-17 Low-energy transmission image of a soft plastic bag that contains simulants and glass bottles. The bag is filled with clothes, shoes, towels, and other *textile* objects.

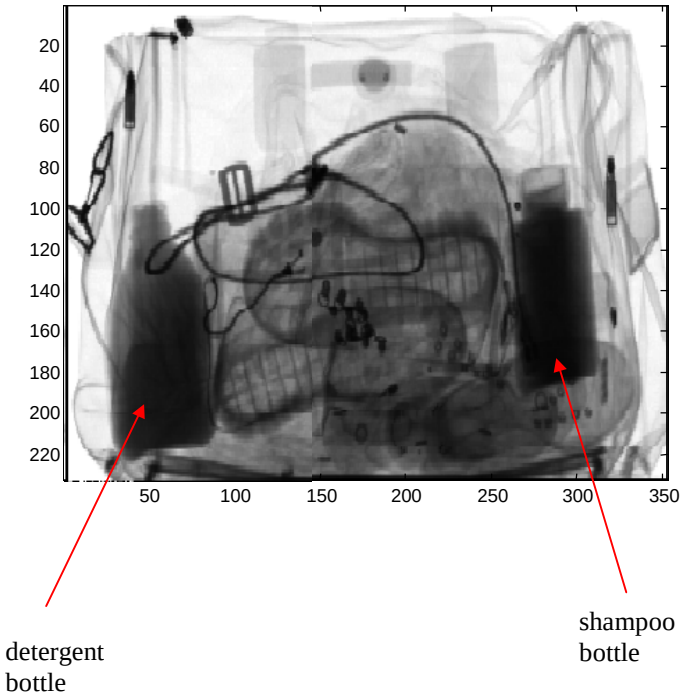

Figure 6-18 Low-energy transmission image of soft plastic bag that contains a shampoo bottle and a detergent bottle. The bag is filled with clothes, towels, shoes, and other daily used objects.

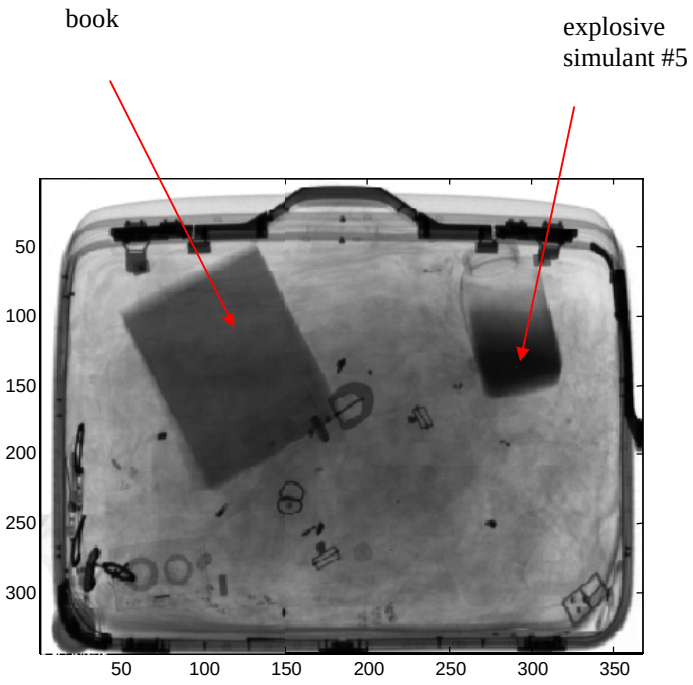

Figure 6-19 Low-energy transmission image of a rigid plastic bag that contains a book and a simulant. The bag is stuffed with clothes and other *textile* objects.

Currently *true_gl()* can only compute the *true* gray levels in transmission modalities. Assume that the image processing system and the material characterization system are fully functioning. That is the *true* gray levels of an object of interest in all four sensing modalities can be computed for an object; and an object's material type can be determined using the *R-L* plane method once knowing the *true* gray levels. Figure 6-20 shows the detection result for this bag. Two objects marked red are the explosive simulants that were correctly identified as illicit materials. In Figure 6-21, the object marked yellow is the object that is suspicious to be made of illicit material.

In summary, the registration and segmentation image-processing system performs well on all tested images. The *true* gray level computation algorithm works well in the transmission modality. The precision of the *true* gray level computation is reasonably high.

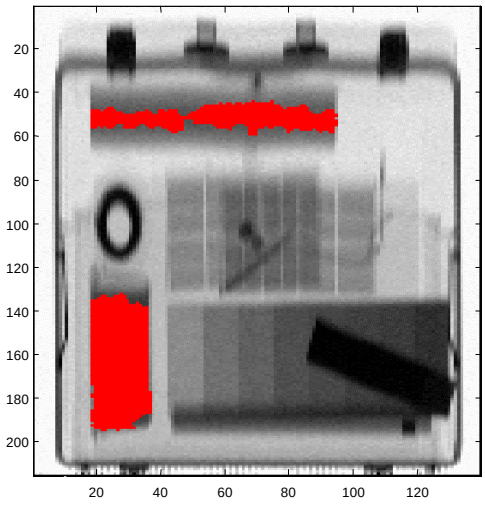

Figure 6-20 Example of a detection result. Two objects have been positively identified as illicit materials.

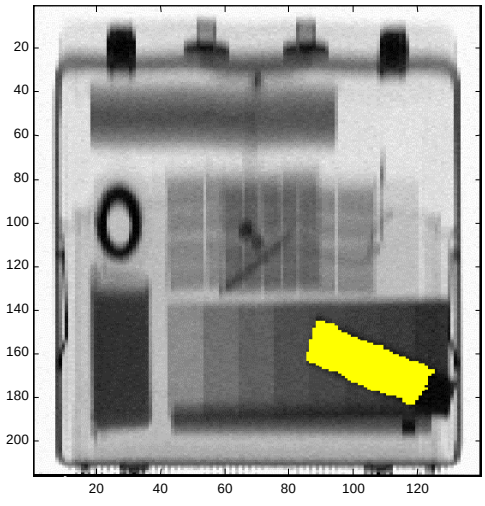

Figure 6-21 Example of a detection result. One object is suspected to be an illicit material.